

A gate-tunable, field-compatible fluxonium

Marta Pita-Vidal,^{1,2} Arno Bargerbos,^{1,2} Chung-Kai Yang,³ David J. van Woerkom,³ Wolfgang Pfaff,³ Nadia Haider,^{1,4} Peter Krogstrup,⁵ Leo P. Kouwenhoven,^{1,3} Gijs de Lange,³ and Angela Kou³

¹*QuTech, Delft University of Technology, 2628 CJ, Delft, The Netherlands*

²*Kavli Institute for Nanoscience, Delft University of Technology, 2628 CJ, Delft, The Netherlands*

³*Microsoft Quantum Lab Delft, 2628 CJ, Delft, The Netherlands*

⁴*Netherlands Organisation for Applied Scientific Research (TNO), 2628 CK, Delft, The Netherlands*

⁵*Center for Quantum Devices, Niels Bohr Institute, University of Copenhagen
and Microsoft Quantum Materials Lab Copenhagen, Denmark*

(Dated: October 17, 2019)

Circuit quantum electrodynamics, where photons are coherently coupled to artificial atoms built with superconducting circuits, has enabled the investigation and control of macroscopic quantum-mechanical phenomena in superconductors [1, 2]. Recently, hybrid circuits incorporating semiconducting nanowires [3–5] and other electrostatically-gateable elements [6–8] have provided new insights into mesoscopic superconductivity [3, 5]. Extending the capabilities of hybrid flux-based circuits to work in magnetic fields would be especially useful both as a probe of spin-polarized Andreev bound states [9–12] and as a possible platform for topological qubits [13–16]. The fluxonium [17] is particularly suitable as a readout circuit for topological qubits [16, 18] due to its unique persistent-current based eigenstates. In this Letter, we present a magnetic-field compatible hybrid fluxonium with an electrostatically-tuned semiconducting nanowire as its non-linear element. We operate the fluxonium in magnetic fields up to 1T and use it to observe the φ_0 -Josephson effect. This combination of gate-tunability and field-compatibility opens avenues for the exploration and control of spin-polarized phenomena using superconducting circuits and enables the use of the fluxonium as a readout device for topological qubits.

The fluxonium consists of a Josephson junction with Josephson energy E_J in parallel with a linear superinductor [19] with inductive energy E_L and a capacitor characterized by the energy E_C , as shown in Fig. 1a. The fluxonium regime ($E_L < E_C < E_J$) is achieved by shunting the junction with a large inductance. This parameter regime results in the eigenstates of the fluxonium being composed of superpositions of persistent currents in multiple directions (Fig. 1b). Since a switch in the parity of a Majorana zero mode (MZM) corresponds to a switch in the direction of the persistent current flowing in the fluxonium circuit, it is uniquely suited to detecting the parity lifetime of a MZM. Building a fluxonium compatible with detecting topological phenomena in a magnetic field, however, presents multiple challenges. The first challenge is reaching the fluxonium regime us-

ing magnetic-field compatible materials. Recent work on magnetic-field compatible materials with a large kinetic inductance such as granular aluminium [20–22] and NbTiN [23–25] has presented a path to meeting the stringent requirements of the fluxonium superinductance.

Here we have realized a fluxonium circuit compatible with MZM-detection as shown in Figs 1c-f. All circuit elements except for the junction are fabricated using NbTiN, which has been demonstrated to have critical fields exceeding 9 T and inductances exceeding 75 pH/□ [24]. The use of NbTiN, however, introduces the possibility of lossy vortices when a magnetic field is applied to the device. We mitigate the effects of these vortices by introducing vortex-pinning holes (inset, Fig. 1c) and using inductances based on thin meanders (Fig. 1e). The small widths of the meanders suppresses the emergence of vortices due to out-of-plane fields, B_x , up to tens of mT [26].

In addition to being composed of magnetic-field compatible materials, for use as a detector, the fluxonium must also maintain its narrow linewidth during the application of a magnetic field. The application of a magnetic field precludes the possibility of using the magnetic shielding necessary for limiting flux noise in flux-based superconducting circuits. We address this challenge by building a gradiometric superinductance as shown in Fig. 1d. Equal fluxes through each of the two loops generate equal currents that are canceled at the junction, rendering the fluxonium insensitive to flux noise due to sources larger than the fluxonium device.

The final challenge is faced when incorporating a semiconducting nanowire into a superconducting circuit. The small junction of the fluxonium is based on a semiconducting InAs nanowire proximitized by an epitaxially-grown aluminum layer (Fig. 1f) [27]. This small junction, however, does not provide a large enough capacitance to achieve the fluxonium regime. We thus add a parallel plate capacitor (blue in Fig. 1d) to achieve the required E_C for the fluxonium. We note that this fluxonium design is flexible enough to incorporate any semiconducting material as its small junction.

We first demonstrate that our device behaves as expected for a fluxonium coupled to a readout resonator. Data from two similar fluxonium devices (device A and device B) will be presented in this Letter. We first focus

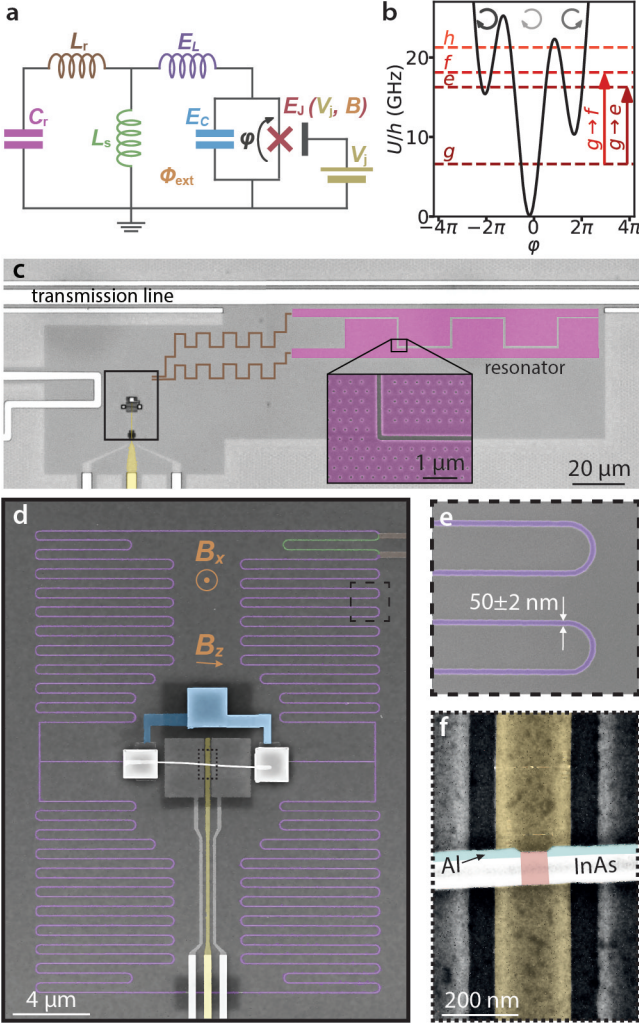


FIG. 1. Nanowire fluxonium. **a**, Circuit model. The fluxonium is composed of a Josephson junction shunted by an inductor and a capacitor. These elements are characterized by the energies E_J , E_L , and E_C , respectively. The value of E_J can be tuned both by the external magnetic field, B , and by the gate voltage, V_j . A readout resonator (constituted by L_r and C_r) is coupled to the fluxonium via a shared inductance L_s . **b**, Potential of the fluxonium (black), determined by E_J and E_L , versus the phase difference across the junction, φ , at $\varphi_{\text{ext}} = 0.2\pi$. The lowest eigenenergies are indicated with horizontal lines. Arrows represent two of the transitions starting from the ground state. **c**, False-colored optical micrograph showing the transmission line and the lumped element resonator, with capacitive and inductive parts shaded in pink and brown respectively. Inset, scanning electron microscope (SEM) image of the resonator's capacitive plates. **d**, SEM image of the fluxonium, corresponding to the area indicated by the box in **c**. The 9 nm-thick NbTiN superinductor (purple, enlarged in **e**), the shared inductance section (green), the parallel plate capacitor (blue) and the nanowire junction (red, enlarged in **f**), correspond, respectively, to the E_L , L_s , E_C and E_J elements in **a**. The out-of-plane component of B , B_x , is used to tune the external magnetic flux Φ_{ext} . B_z is the component parallel to the wire.

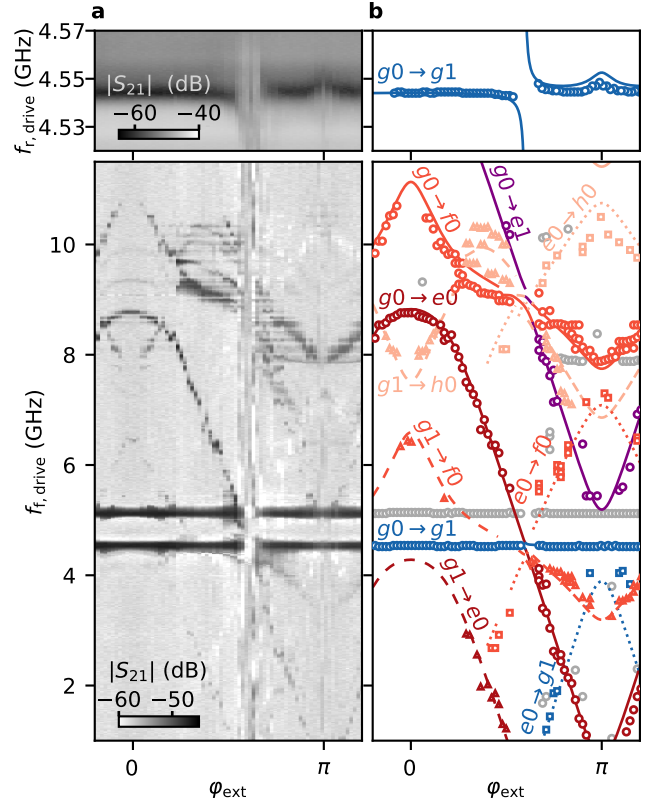


FIG. 2. Two-tone spectroscopy of device A, at $B_z = 0$. **a**, Magnitude of the transmitted readout signal as a function of the external flux and $f_{r,\text{drive}}$ (top) and $f_{f,\text{drive}}$ (bottom), showing the flux modulation of the different transitions. **b**, Extrema extracted from **a** (markers) and fitted transition frequencies (lines) obtained from the numerical diagonalization of the model Hamiltonian (Methods). Gray markers indicate extrema that are not associated with any fluxonium-resonator transitions. A value of $E_J/h = 6.7$ GHz is extracted from the fit.

on the behavior of device A. We monitored the transmission amplitude, $|S_{21}|$, at frequencies $f_{r,\text{drive}}$ around the resonator frequency $f_{g_0 \rightarrow g_1}$, as a function of the external phase $\varphi_{\text{ext}} = \frac{2e}{h} \Phi_{\text{ext}}$, as shown in the top panel of Fig. 2a. Transitions are labelled as $m_i n_i \rightarrow m_e n_e$, where m_i (m_e) and n_i (n_e) are the initial (end) states of the fluxonium and resonator, respectively. The resonator spectrum is periodic in flux and also exhibits gaps in its visibility, which indicate that the resonator is coupled to the fluxonium. The bottom panel in Fig. 2a shows the flux dependence of the observed transition frequencies of the fluxonium-resonator system, measured by monitoring the transmission amplitude at $f_{r,\text{drive}} = f_{g_0 \rightarrow g_1}$ while the system is driven with a second tone with frequency $f_{f,\text{drive}}$, also via the resonator. Threading a flux quantum through the gradiometric loop that comprises the fluxonium corresponds to $B_x = 550 \mu\text{T}$, which is much greater than the $15 \mu\text{T}$ that would be needed to thread a flux quantum through one of the two symmetric loops. The gradiometric geometry thus reduces the sensitivity

of the fluxonium to magnetic field noise larger than the fluxonium loop by more than an order of magnitude. The residual asymmetry present is due to the nanowire placement and the presence of the gates and capacitor inside the loop.

To fit the spectroscopy data (markers in Fig. 2b), we diagonalize the Hamiltonian for the circuit shown in Fig. 1a [28], leaving all circuit parameters free except for $C_r = 26$ fF, which we extract from electromagnetic simulations. The parameters obtained from the fit are shown in Tab. I and the fitted transition frequencies are denoted with lines in Fig. 2b. Each state is identified by the closest state in energy for the uncoupled system. In addition to transitions originating from the ground state, $g0$, we also observe transitions for which the initial state is $g1$, with one photon in the resonator (dashed lines). This is due to the continuous drive used to monitor $|S_{21}|$ at $f_{g0 \rightarrow g1}$, which can populate the resonator. Transitions starting from the first excited fluxonium state, $e0$, around $\varphi_{\text{ext}} = \pi$ (dotted lines) are also observed. The transition frequency for $g0 \rightarrow e0$ goes below 1 GHz near $\varphi_{\text{ext}} = \pi$. The transitions from $e0$ thus occur due to the expected equilibrium thermal occupation of $e0$ for temperatures of around 20 mK. We find excellent agreement between the experimental data and the fit, with all fit parameters coming to within 5% of the designed parameters.

Mesoscopic phenomena such as Majorana zero modes often require fine tuning of the density in the semiconductor. We here demonstrate that the spectrum of the fluxonium is measurable over a large range of gate voltages and thus does not limit the possible observable phenomena. We first measure $f_{g0 \rightarrow g1}$ versus V_j . As shown in Fig. 3a, the resonator frequency is constant at low and high voltage values but has non-monotonic fluctuations in an intermediate range, which is consistent with observations in previous experiments on nanowire junctions [3, 4]. Figures 3b, c and d present spectra taken at three different V_j values (marked by solid lines in 3a). Here we use a lower drive power than in Fig. 2 to reduce broadening of the spectral lines due to the drive power, therefore the main observable transitions start from the ground state, $g0$. For low V_j , we observe a weakly anharmonic spectrum (Fig. 3b). For large V_j values (Figs. 3c,d), however, the flux dependence and the anharmonicity become much stronger. We also note the presence of additional transitions in the spectroscopy data for intermediate and large V_j denoted by the lighter markers in Fig. 3c and

d. The spectra at intermediate V_j is taken at a point where the junction is very sensitive to gate voltage; the additional transitions are due to the E_J of the junction fluctuating while the spectroscopy is being performed. At higher V_j , the E_J of the junction is stable as a function of gate but additional transitions due to the presence of the resonator drive are also observed. We fit the data of the three spectra using the same parameters as those used in Fig. 2 while only allowing E_J to vary. The fits maintain their accuracy over the whole V_j range. We therefore conclude that E_J is the only circuit parameter affected by large changes in V_j . Our results thus show that it is possible to address and observe the state of the system over a large E_J -range encompassing regimes where its eigenstates are of very different character.

Next, we explore the magnetic field compatibility of the nanowire fluxonium. The magnetic field behavior of the device strongly depends on the microscopic details of the nanowire junction. In order to demonstrate the field compatibility of the fluxonium circuit elements, we here show data from device B whose parameters were optimized for magnetic field compatibility. The magnetic field behavior of device A is provided in the supplement. Spectroscopy measurements at two different V_j and B_z points are shown in Figs. 4a and b. We continue to be able to perform spectroscopy on the fluxonium over the full range in φ_{ext} at fields up to 1 T. We do note, however, that at higher magnetic fields, the thermal occupation of the excited state of the fluxonium does appear to be higher since we observe transitions from this state even when the $g0 \rightarrow e0$ frequency is above 1 GHz. Importantly, we can still fit the spectroscopy data accurately in this regime, indicating that the fluxonium-resonator Hamiltonian remains valid at high magnetic fields, with E_J being the only parameter largely affected by B_z . Fit parameters for device B are shown in Tab. I.

We finally use the nanowire fluxonium to investigate the behaviour of spin-orbit coupled semiconducting junctions in magnetic field. We perform spectroscopy measurements at gate voltages ranging from 3.5 to 4.8 V and fields ranging from 0 to 1 T. From the spectroscopy we extract E_J as a function of B_z at two different gate points, which is shown in Fig. 4c. A non-monotonic decrease of E_J with field is observed at both gate points. We expect an overall decrease in E_J versus B_z due to the superconducting gap closing at high magnetic fields. The non-monotonic behaviour of E_J , however, suggests the presence of interference between different modes in the junction [29].

A shifting of the zero-flux point in the spectroscopy of the fluxonium device at high fields can be used to determine the breaking of multiple symmetries in the semiconducting junction [30]. This phase shift is known as the φ_0 -Josephson effect, which occurs when chiral and time-reversal symmetries are both broken in the junction. In InSb- and InAs-based junctions, this symmetry-breaking originates from the interplay between the presence of multiple channels in the junction, spin-orbit coupling,

	Device A	Device B
E_C/h (GHz)	2.35	1.75
E_L/h (GHz)	0.7	1.1
C_r (fF)	26	26
L_r (nH)	47	42
L_s (nH)	8.0	4.5

TABLE I. Device parameters obtained by fitting spectra in figures 2, 3 and 4 and by electromagnetic simulations. h is Planck's constant.

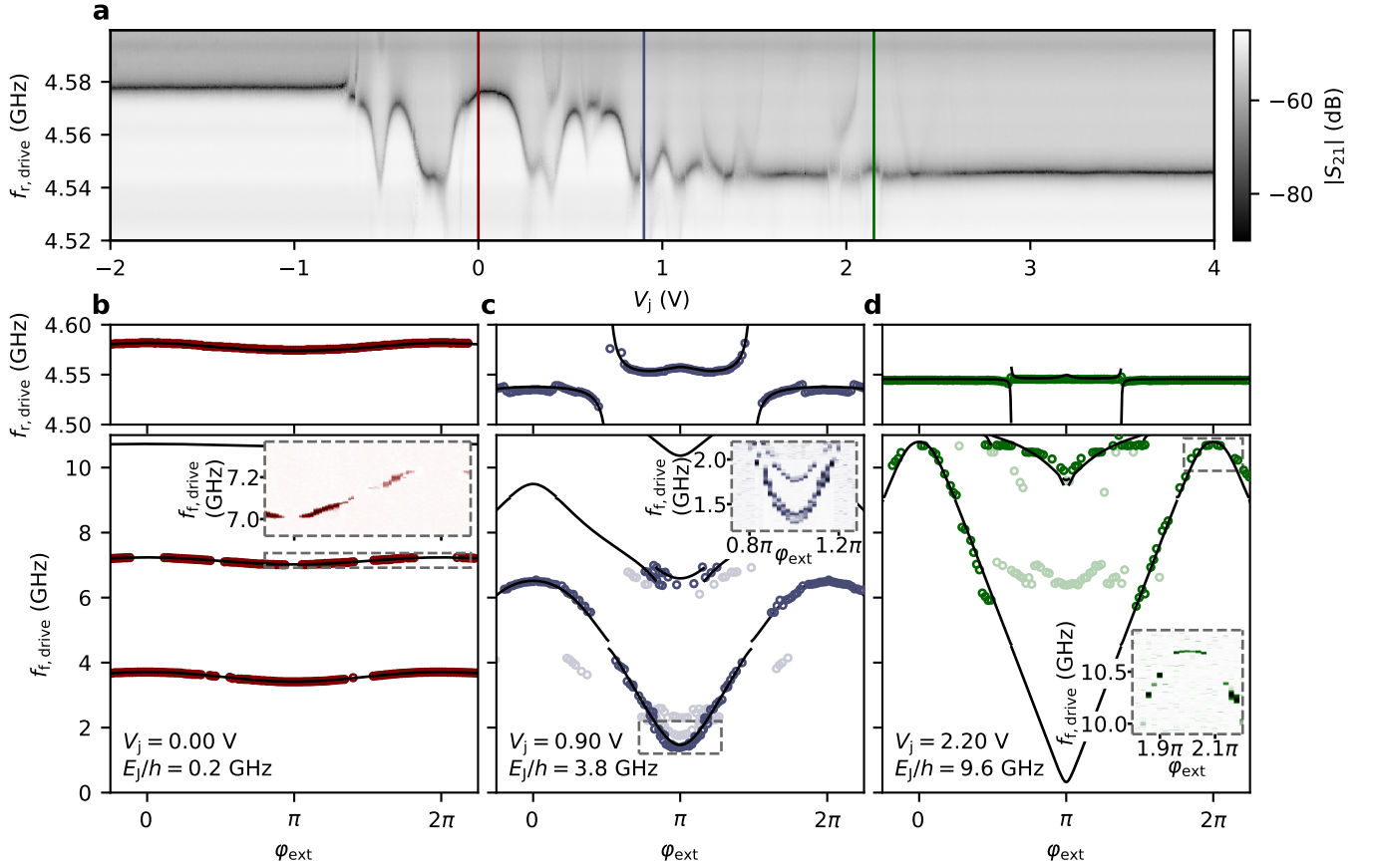


FIG. 3. **Gate tuning of E_J in device A, at $B_z = 0$.** **a**, Gate dependence of the resonator's resonant frequency, $f_{g0 \rightarrow g1}$, at $\varphi_{\text{ext}} = 1.25\pi$. **b-d**, Fluxonium spectra at three different gate points, indicated with vertical lines in **a**. The markers correspond to the peaks extracted from the measured resonator (top) and two-tone (bottom) transmission data. The fitted transition frequencies $f_{g0 \rightarrow e0}$, $f_{g0 \rightarrow f0}$ and $f_{g0 \rightarrow h0}$ (black lines) are obtained by fitting the darker markers. The values of E_J/h extracted are 0.2, 3.8 and 9.6 GHz respectively. The insets in **b**, **c** and **d** show sections of the measured transmission magnitude. In **b** we observe gaps in visibility at zero and half flux in the $g0 \rightarrow f0$ transition.

and the Zeeman splitting due to the applied magnetic field [30–32]. We observe such a shift in the zero-flux point of the spectroscopy lines as V_J is varied in a B_z field (indicated by φ_0 in Fig. 4a.) The φ_0 -shift as a function of V_J is shown, at $B_z = 0$ and at $B_z = 0.5$ T, in Fig. 4d; the φ_0 value at $V_J = 4.80$ V is taken as the $\varphi_0 = 0$ reference. At $B_z = 0$ the zero-flux point does not change, while it changes continuously with V_J when a B_z field is applied. We remark that since the observed phase shift appears as a function of V_J at fixed magnetic fields, we can exclude trivial effects such as misalignment of the magnetic field.

In conclusion, we have successfully realized a gate-tunable fluxonium resilient to high magnetic fields. We have combined a gate-controlled junction with magnetic field-compatible materials and a novel gradiometric design to build the hybrid fluxonium. We are able to perform spectroscopy over a large range of gate voltages and

in-plane magnetic fields. We have used the fluxonium to investigate the behavior of an InAs Josephson junction in a magnetic field and observed a non-monotonic decrease of the E_J of the junction as well as the φ_0 -Josephson effect.

Our magnetic-field compatible hybrid fluxonium can now be used as a detector for the 4π -periodic Josephson effect [18] and of Majorana parity dynamics. We emphasize that the hybrid fluxonium is not limited to the exploration of nanowires but constitutes a new platform for exploring the behavior of topological materials as well as superconductivity in the presence of a magnetic field. Proposals to probe superconductor-proximitized edge states in a quantum spin Hall insulator [33, 34] or field-dependent spin-polarized correlated insulating phases [35] are also now accessible using our hybrid circuit.

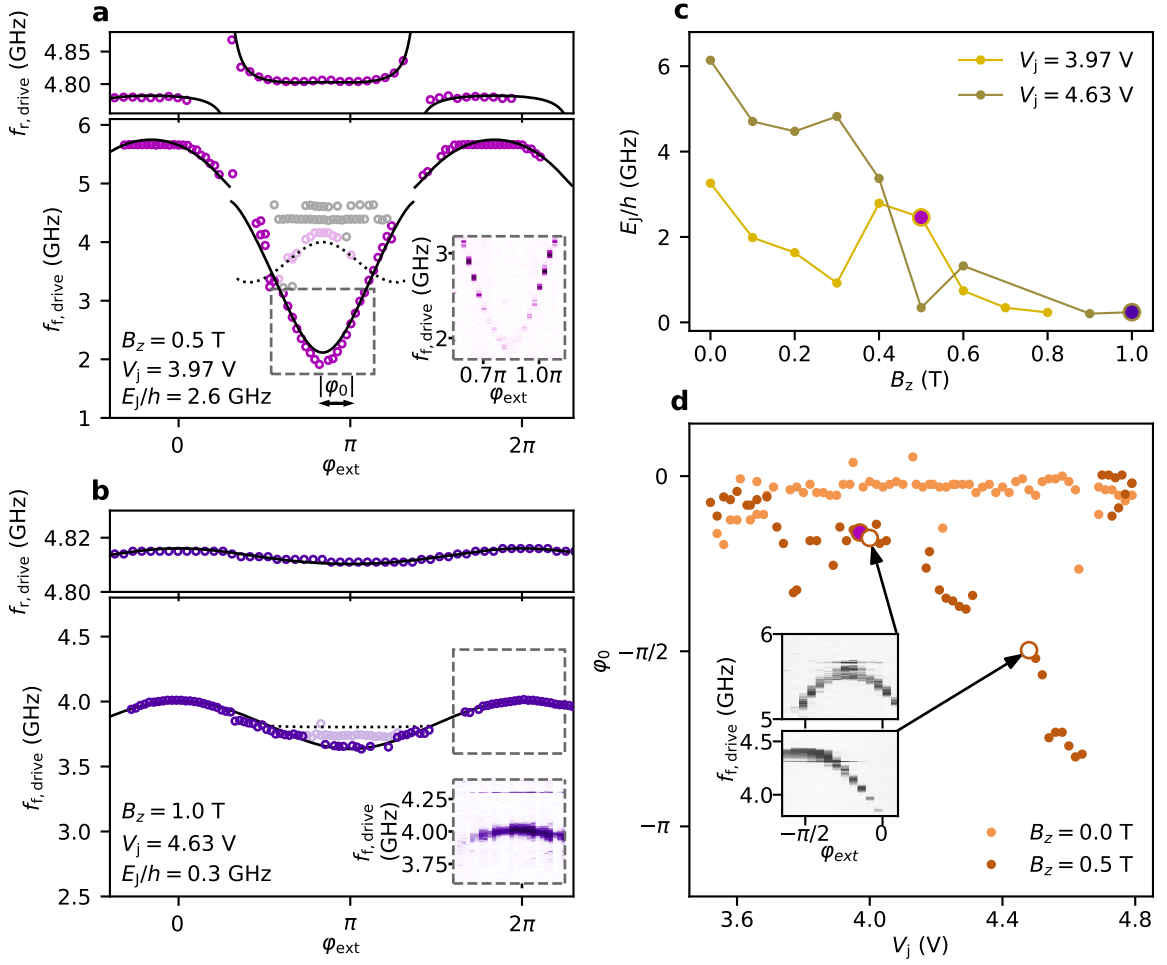


FIG. 4. **Behavior of device B in magnetic field.** **a, b,** Fluxonium spectra at two different V_j and B_z points. The E_J value extracted from the fit is lower at higher magnetic field. In **a** we observe a $\varphi_0 = -0.16\pi$ phase shift with respect to a reference φ_{ext} taken at the same field at $V_j = 4.80$ V. **c,** E_J versus B_z at two different gate voltage points. E_J decreases non-monotonically with field. **d,** φ_0 versus V_j at two different magnetic field points. At $B_z = 0.0$ T, φ_0 stays constant for the whole V_j range. At $B_z = 0.5$ T, however, there is a continuous φ_0 shift that ranges from 0 to $-\pi$. The two insets show the zero-flux spectroscopy feature shifted from zero at two different gate points. In **c** and **d**, the points corresponding to the spectra in **a** and **b** are highlighted with matching colors.

- quantum computation. *Phys. Rev. A* **69**, 062320 (2004).
- [2] Chiorescu, I. *et al.* Coherent dynamics of a flux qubit coupled to a harmonic oscillator. *Nature* **431**, 159–162 (2004).
- Wallraff, A. *et al.* Strong coupling of a single photon to a superconducting qubit using circuit quantum electrodynamics. *Nature* **431**, 162–167 (2004).
- [3] de Lange, G. *et al.* Realization of microwave quantum circuits using hybrid superconducting-semiconducting nanowire Josephson elements. *Phys. Rev. Lett.* **115**, 127002 (2015).
- Larsen, T. W. *et al.* Semiconductor-nanowire-based superconducting qubit. *Phys. Rev. Lett.* **115**, 127001 (2015).
- [4] Luthi, F. *et al.* Evolution of nanowire transmon qubits and their coherence in a magnetic field. *Phys. Rev. Lett.* **120**, 100502 (2018).
- [5] Hays, M. *et al.* Direct microwave measurement of Andreev-bound-state dynamics in a semiconductor-nanowire Josephson junction. *Phys. Rev. Lett.* **121**, 047001 (2018).
- [6] Mi, X., Cady, J. V., Zajac, D. M., Deelman, P. W. & Petta, J. R. Strong coupling of a single electron in silicon to a microwave photon. *Science* **355**, 156–158 (2017).
- [7] Casparis, L. *et al.* Superconducting gatemon qubit based on a proximitized two-dimensional electron gas. *Nature Nanotechnology* **13**, 915–919 (2018).
- [8] Kroll, J. G. *et al.* Magnetic field compatible circuit quantum electrodynamics with graphene Josephson junctions. *Nature Communications* **9**, 4615 (2018).
- Wang, J. I.-J. *et al.* Coherent control of a hybrid superconducting circuit made with graphene-based van der waals heterostructures. *Nature Nanotechnology* **14**, 120–125 (2019).
- [9] Zazunov, A., Brunetti, A., Yeyati, A. L. & Egger, R. Quasiparticle trapping, Andreev level population dynamics, and charge imbalance in superconducting weak links. *Phys. Rev. B* **90**, 104508 (2014).

- [10] Vayrynen, J. I., Rastelli, G., Belzig, W. & Glazman, L. I. Microwave signatures of Majorana states in a topological Josephson junction. *Phys. Rev. B* **92**, 134508 (2015).
- [11] van Heck, B., Vayrynen, J. I. & Glazman, L. I. Zeeman and spin-orbit effects in the Andreev spectra of nanowire junctions. *Phys. Rev. B* **96**, 075404 (2017).
- [12] Yavilberg, K., Ginossar, E. & Grosfeld, E. Differentiating Majorana from Andreev Bound States in a Superconducting Circuit. Preprint at <https://arxiv.org/abs/1902.07229> (2019).
- [13] Hassler, F., Akhmerov, A. R. & Beenakker, C. W. J. The top-transmon: a hybrid superconducting qubit for parity-protected quantum computation. *New Journal of Physics* **13**, 095004 (2011).
- [14] Hyart, T. *et al.* Flux-controlled quantum computation with Majorana fermions. *Phys. Rev. B* **88**, 035121 (2013).
- [15] Ginossar, E. & Grosfeld, E. Microwave transitions as a signature of coherent parity mixing effects in the Majorana-transmon qubit. *Nature Communications* **5**, 4772 (2014).
- [16] Stenger, J. P. T., Hatridge, M., Frolov, S. M. & Pekker, D. Braiding quantum circuit based on the 4π Josephson effect. *Phys. Rev. B* **99**, 035307 (2019).
- [17] Manucharyan, V. E., Koch, J., Glazman, L. I. & Devoret, M. H. Fluxonium: Single Cooper-pair circuit free of charge offsets. *Science* **326**, 113–116 (2009).
- [18] Pekker, D., Hou, C.-Y., Manucharyan, V. E. & Demler, E. Proposal for coherent coupling of Majorana zero modes and superconducting qubits using the 4π Josephson effect. *Phys. Rev. Lett.* **111**, 107007 (2013).
- [19] Manucharyan, V. E. *Superinductance*. Ph.D. thesis, Yale University (2012). URL [http://qulab.eng.yale.edu/documents/theses/Manucharyan,%20Vladimir%20-%20Superinductance%20\(Yale,%202012\).pdf](http://qulab.eng.yale.edu/documents/theses/Manucharyan,%20Vladimir%20-%20Superinductance%20(Yale,%202012).pdf).
- [20] Rotzinger, H. *et al.* Aluminium-oxide wires for superconducting high kinetic inductance circuits. *Superconductor Science and Technology* **30**, 025002 (2016).
- [21] Grunhaupt, L. *et al.* Loss mechanisms and quasiparticle dynamics in superconducting microwave resonators made of thin-film granular aluminum. *Phys. Rev. Lett.* **121**, 117001 (2018).
- [22] Maleeva, N. *et al.* Circuit quantum electrodynamics of granular aluminum resonators. *Nature Communications* **9**, 3889 (2018).
- [23] Annunziata, A. J. *et al.* Tunable superconducting nanoinductors. *Nanotechnology* **21**, 445202 (2010).
- [24] Samkharadze, N. *et al.* High-kinetic-inductance superconducting nanowire resonators for circuit QED in a magnetic field. *Phys. Rev. Applied* **5**, 044004 (2016).
- [25] Hazard, T. M. *et al.* Nanowire superinductance fluxonium qubit. *Phys. Rev. Lett.* **122**, 010504 (2019).
- [26] Clem, J. R. Vortex Exclusion from Superconducting Strips and SQUIDS in Weak Perpendicular Ambient Magnetic Fields. *APS March Meeting Abstracts* K36.06 (1998).
- [27] Krogstrup, P. *et al.* Epitaxy of semiconductor-superconductor nanowires. *Nature Materials* **14**, 400 EP – (2015). Article.
- [28] Smith, W. C. *et al.* Quantization of inductively shunted superconducting circuits. *Phys. Rev. B* **94**, 144507 (2016).
- [29] Zuo, K. *et al.* Supercurrent interference in few-mode nanowire Josephson junctions. *Phys. Rev. Lett.* **119**, 187704 (2017).
- [30] Yokoyama, T., Eto, M. & Nazarov, Y. V. Anomalous Josephson effect induced by spin-orbit interaction and Zeeman effect in semiconductor nanowires. *Phys. Rev. B* **89**, 195407 (2014).
- [31] Szombati, D. B. *et al.* Josephson ϕ_0 -junction in nanowire quantum dots. *Nature Physics* **12**, 568 EP – (2016).
- [32] van Woerkom, D. J. *et al.* Microwave spectroscopy of spinful Andreev bound states in ballistic semiconductor Josephson junctions. *Nature Physics* **13** (2017).
- [33] Dolcini, F., Houzet, M. & Meyer, J. S. Topological Josephson ϕ_0 junctions. *Phys. Rev. B* **92**, 035428 (2015).
- [34] Wu, S. *et al.* Observation of the quantum spin hall effect up to 100 kelvin in a monolayer crystal. *Science* **359**, 76–79 (2018).
- [35] Cao, Y. *et al.* Electric Field Tunable Correlated States and Magnetic Phase Transitions in Twisted Bilayer-Bilayer Graphene. Preprint at <https://arxiv.org/abs/1903.08596> (2019). Liu, X. *et al.* Spin-polarized Correlated Insulator and Superconductor in Twisted Double Bilayer Graphene. Preprint at <https://arxiv.org/abs/1903.08130> (2019).

ACKNOWLEDGEMENTS

We thank W. Uilhoorn for fabrication advice. We also thank B. van Heck and A. Antipov for helpful discussions. This research was co-funded by the allowance for Top consortia for Knowledge and Innovation (TKI’s) from the Dutch Ministry of Economic Affairs and the Microsoft Quantum initiative.

AUTHOR CONTRIBUTIONS

M.P.-V., G.d.L. and A.K. conceived the experiment. M.P.-V., A.B., and N.H. performed device simulations. M.P.-V., D.J.v.W. and C.-K.Y. fabricated the devices. M.P.-V. performed the measurements and analysed the data with input from W.P., L.P.K., and A.K. P.K. grew the InAs nanowires. M.P.-V. and A.K. wrote the manuscript with input from all authors.

METHODS

Materials and fabrication details

All circuit elements, except the Josephson junction, are fabricated using a 9 nm-thick sputtered NbTiN film, with a kinetic inductance of 41 pH/ \square . The elements are defined by e-beam lithography and reactive ion etching. The superinductive loop of the fluxonium is made with a 50 nm-wide NbTiN strip line and has a total inductance of ~ 100 nH. The fluxonium capacitor consists of two square NbTiN plates sandwiching a 29 nm-thick PECVD SiN dielectric. The junction is based on a semiconducting InAs nanowire with an epitaxially grown Al layer. The

nanowire is deterministically deposited on top of the pre-patterned leads of the inductor and capacitor using a micromanipulator. The Josephson junction is defined by etching away an Al section of around 80 nm on top of the junction gate. The wire is contacted to the leads using 150 nm-thick sputtered NbTiN.

The fluxonium is inductively coupled to a readout LC-resonator by a small shared inductance L_s . The resonator (shown in Fig. 1b) is composed of a lumped element capacitor with vortex-pinning holes and an inductor formed from a 200 nm-wide meandering strip. The gate and transmission lines are made out of 100 nm-thick sputtered NbTiN. The resonator is capacitively coupled to a transmission line to allow readout of the fluxonium using standard dispersive readout techniques.

Fitting procedure

To find the relative extrema we apply a peak finding algorithm to the raw data. This algorithm first smooths the data in the frequency axis to avoid errors in peak finding due to noise. A minimum peak height is specified.

We fit the extracted data with the Hamiltonian corresponding to the circuit model in Fig. 1. The fluxonium Hamiltonian, \hat{H}_f , and the total Hamiltonian of the coupled readout-fluxonium system, \hat{H} , can be written in terms of two degrees of freedom, $\hat{\varphi}_f$ and $\hat{\varphi}_r$ (the phase drops across the fluxonium junction and across

C_r , respectively), and their conjugated charges \hat{n}_f and \hat{n}_r [28]. In the limit $L_f \gg L_s, L_r$ (where $L_f = \frac{\Phi_0^2}{4\pi^2 E_L}$ and $\Phi_0 = h/2e$),

$$\hat{H}_f = 4E_C \hat{n}_f^2 - E_J(V_J, B) \cos(\hat{\varphi}_f) + \frac{1}{2} E_L (\hat{\varphi}_f - \varphi_{\text{ext}})^2 \quad (1)$$

and

$$\hat{H} = \frac{2e^2}{C_r} \hat{n}_r^2 + \frac{1}{2} \frac{(\Phi_0/2\pi)^2}{(L_r + L_s)} \hat{\varphi}_r^2 - \frac{1}{2} \frac{(\Phi_0/2\pi)^2 L_s}{L_f(L_r + L_s)} \hat{\varphi}_r \hat{\varphi}_f + \hat{H}_f. \quad (2)$$

The first two terms of \hat{H} describe the uncoupled resonator, while the third term accounts for the coupling between resonator and fluxonium.

We diagonalize Hamiltonian 2 using the numerical method in [28]. All the spectra for the same device are fitted simultaneously. The free parameters E_C , E_L , L_r and L_s are common for all spectra corresponding to the same device. The free parameter E_J , however, has a different value for each spectrum.

All markers shown in Figures 2, 3 and 4 are included without distinction in the fits. The markers colors are assigned by association to the different transitions. Grey markers do not correspond to any transition present in the fit.

Supplementary information for “A gate-tunable, field-compatible fluxonium”

Marta Pita-Vidal,^{1,2} Arno Bargerbos,^{1,2} Chung-Kai Yang,³ David J. van Woerkom,³ Wolfgang Pfaff,³ Nadia Haider,^{1,4} Peter Krogstrup,⁵ Leo P. Kouwenhoven,^{1,3} Gijs de Lange,³ and Angela Kou³

¹*QuTech, Delft University of Technology, 2628 CJ, Delft, The Netherlands*

²*Kavli Institute for Nanoscience, Delft University of Technology, 2628 CJ, Delft, The Netherlands*

³*Microsoft Quantum Lab Delft, 2628 CJ, Delft, The Netherlands*

⁴*Netherlands Organisation for Applied Scientific Research (TNO), 2628 CK, Delft, The Netherlands*

⁵*Center for Quantum Devices, Niels Bohr Institute, University of Copenhagen
and Microsoft Quantum Materials Lab Copenhagen, Denmark*

(Dated: October 17, 2019)

I. THEORETICAL MODEL FOR THE UNCOUPLED FLUXONIUM

The Hamiltonian for the uncoupled fluxonium, \hat{H}_f , can be written in terms of the phase drop across the junction, $\hat{\varphi}_f$, and its conjugated charge \hat{n}_f [1, 2]

$$\hat{H}_f = 4E_C\hat{n}_f^2 - E_J(V_J, B)\cos(\hat{\varphi}_f) + \frac{1}{2}E_L(\hat{\varphi}_f - \varphi_{\text{ext}})^2. \quad (1)$$

Each of the terms in \hat{H}_f results from one of the three characteristic energies of fluxonium: E_C , E_L and E_J . The two conjugated variables in this Hamiltonian, $\hat{\varphi}_f$ and \hat{n}_f , are analogous to position and momentum, respectively. With this interpretation, the two terms involving $\hat{\varphi}_f$ constitute a phase-dependent potential

$$V(\varphi) = -E_J\cos(\varphi) + \frac{1}{2}E_L(\varphi - \varphi_{\text{ext}})^2. \quad (2)$$

Fig. 1i shows the potential at $\varphi_{\text{ext}} = 0$ for the three E_J values in Fig. 3 in the main text. The E_L term results in a parabolic background, common for the three cases. The E_J adds a periodic modulation on top of it, which becomes more noticeable as E_J increases. E_C can be seen as a mass term and, together with the potential V , determines the eigenstates of fluxonium. The lowest energy eigenstates are labelled g , e , f and h . Their energies at $\varphi_{\text{ext}} = 0$ are shown as colored lines in Fig. 1i. Fig. 1ii shows how these energies disperse with φ_{ext} . For small E_J values, the variation of φ_{ext} results in weak oscillations of the eigenenergies, while for large E_J 's the φ_{ext} -dependence is much stronger. In the limit of small E_J the eigenstates are vibrational modes of the harmonic LC oscillator determined by E_L and E_C . Therefore, their energies are evenly spaced with a separation determined by the plasma frequency $\sqrt{8E_CE_L}/h$. In the limit of large E_J the eigenstates become superpositions of persistent currents localized in phase.

Fig. 1iii shows the transition frequencies between different pairs of eigenstates, which are the quantities that can be addressed experimentally. For simplicity, only the transitions starting from the ground state are shown here. The two-tone spectroscopy data in Figures 2, 3 and 4 in the main text shows the measured transition frequencies for the fluxonium-resonator coupled system.

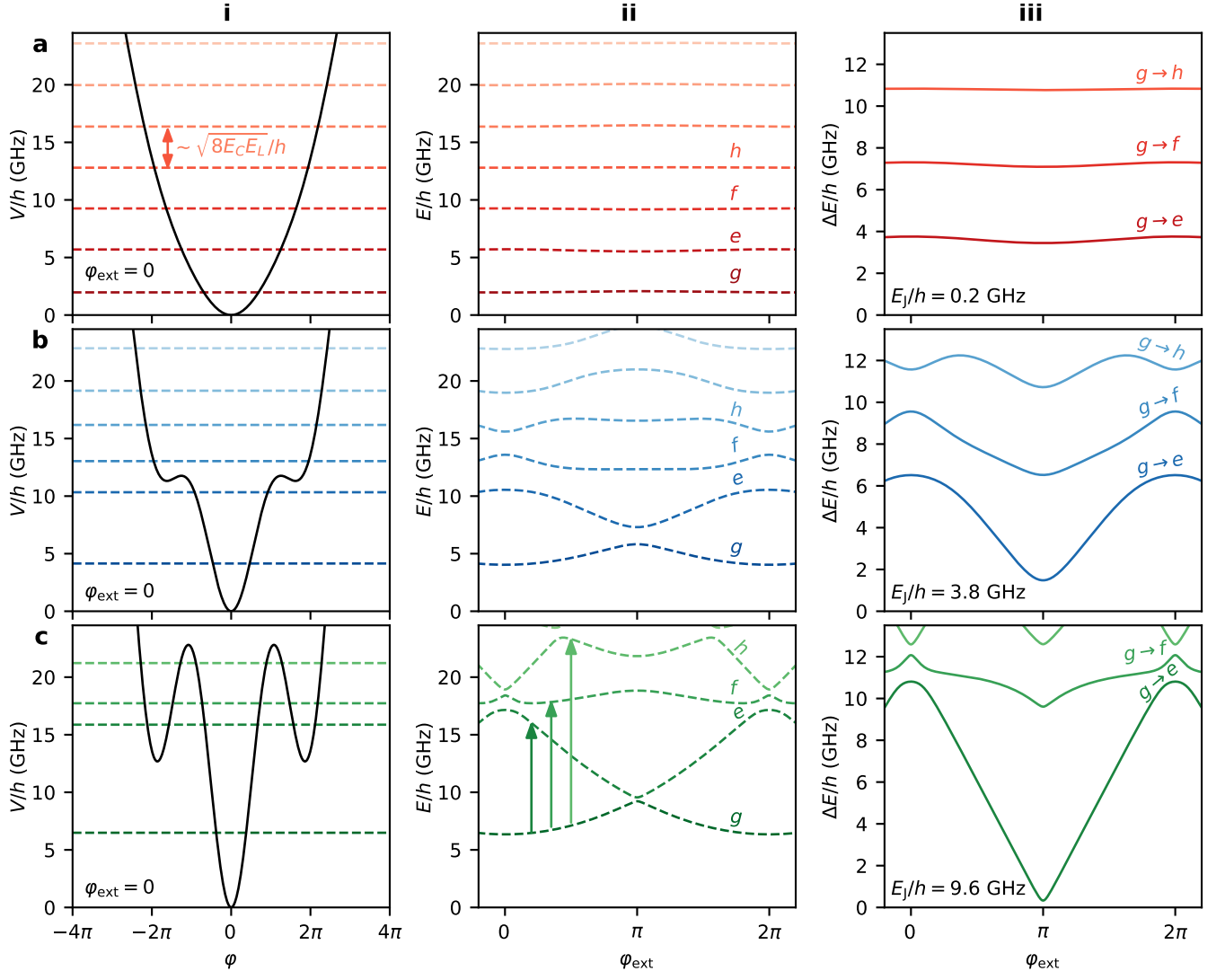


FIG. 1. **Potential, energy spectrum and transition frequencies of the uncoupled fluxonium.** Rows **a**, **b** and **c** correspond to $E_J/h = 0.2, 3.8$ and 9.6 GHz, respectively, for the model parameters of device A. Column **i** shows the fluxonium potential in equation 2, at $\phi_{\text{ext}} = 0$, in black lines. The lowest eigenenergies of Hamiltonian 1 at $\phi_{\text{ext}} = 0$ are superimposed as horizontal dashed lines. Column **ii** shows how these energies disperse as ϕ_{ext} is varied. The solid arrows indicate transitions starting from the ground state, g . The energies of these transitions are plotted in column **iii** as a function of ϕ_{ext} .

II. FIELD DATA FOR DEVICE A

Fig. 2 shows the spectroscopy data for device A under in-plane magnetic field, up to 0.3 T. We note the presence of phase-independent lines crossing the fluxonium spectrum at frequencies above 6 GHz at 0.3 T. Beyond 0.3 T, the transition frequencies of the fluxonium came within 1 GHz of the resonator frequency, which resulted in the spectroscopy of the fluxonium becoming unmeasurable.

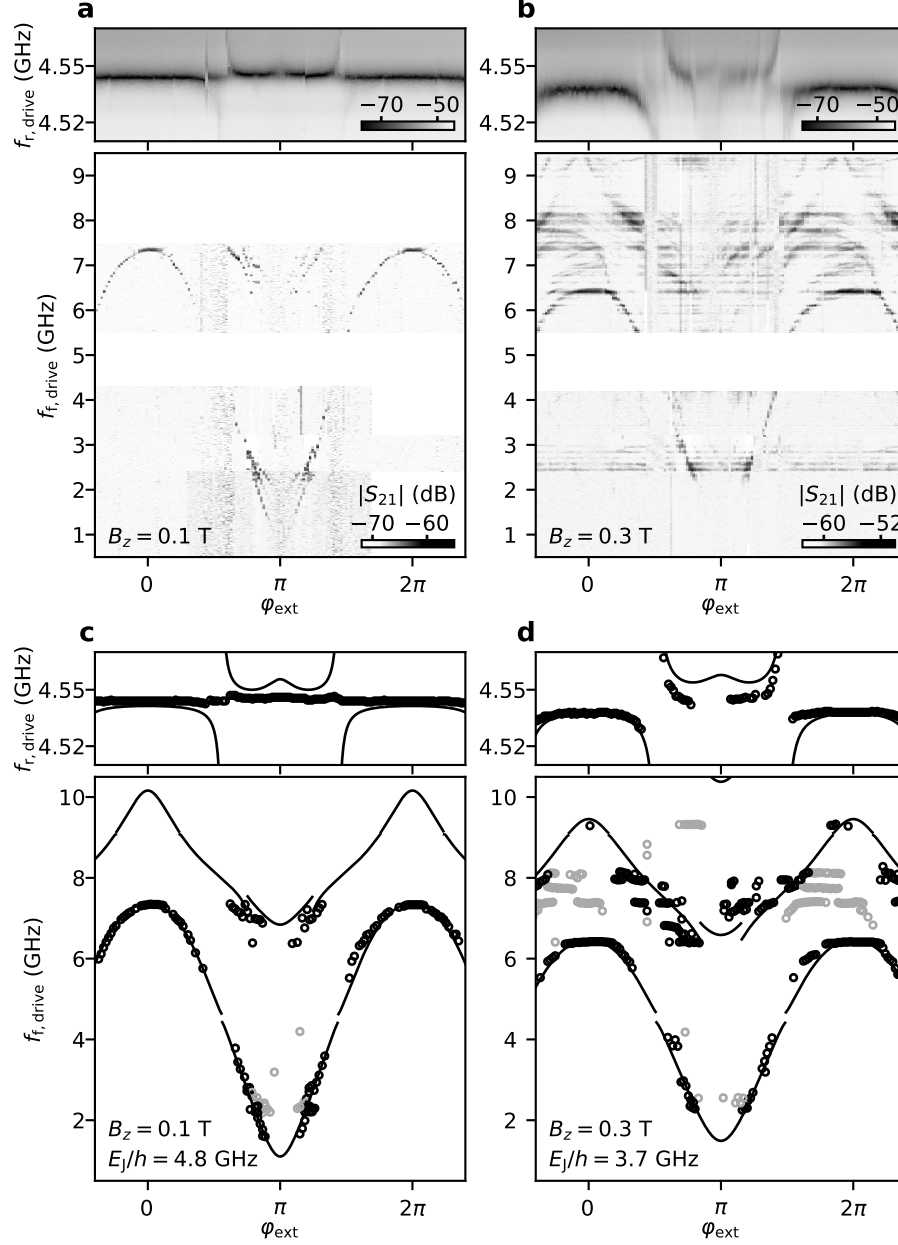


FIG. 2. **Spectroscopy data for device A under in-plane magnetic field.** Spectra in **a** and **b** are taken at $B_z = 0.1$ T and 0.3 T, respectively, at the same gate voltage, $V_j = 2.20$ V, as the spectrum in Fig. 3c in the main text. **c** and **d** show the extracted peaks (markers) and the fitted transition frequencies (solid lines). The E_J/h values obtained from the fit are 4.8 and 3.7 GHz, respectively.

III. ADDITIONAL FIELD AND GATE DATA FOR DEVICE B

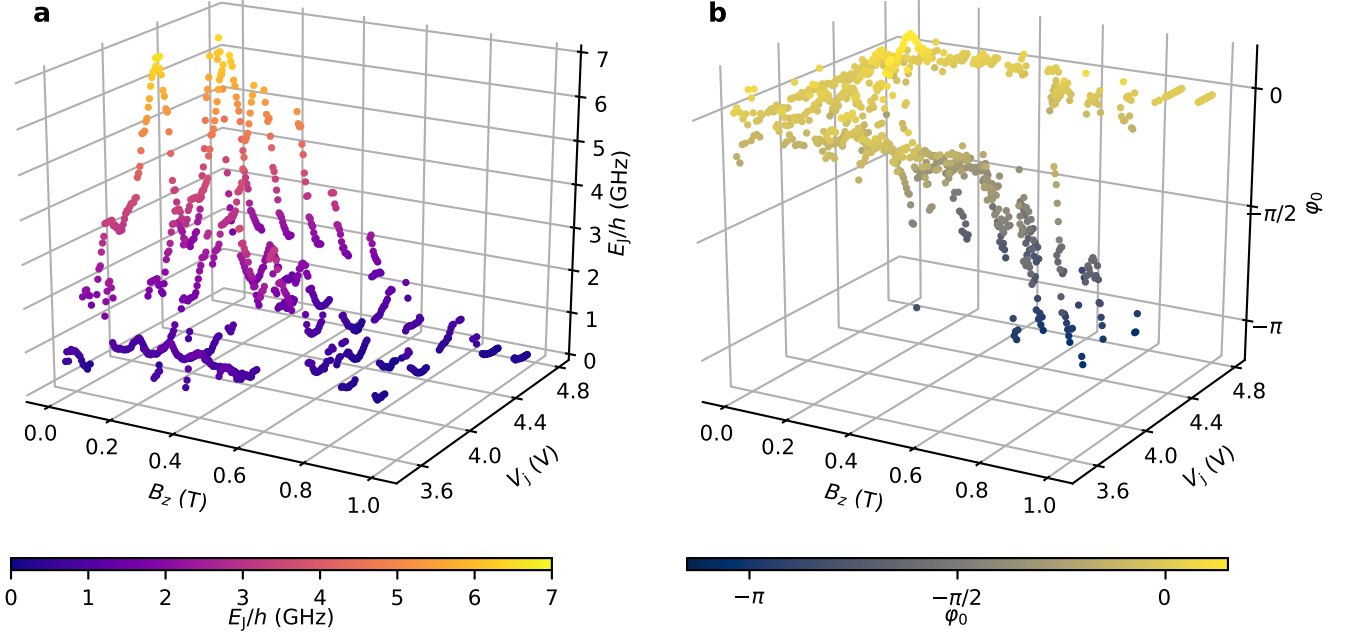


FIG. 3. **Extra data for device B in magnetic field.** **a** E_J versus B_z and V_j . The data shown in Fig. 4c in the main text corresponds to two line-cuts at $V_j = 3.97$ V and $V_j = 4.63$ V. **b** ϕ_0 versus B_z and V_j . The data shown in Fig. 4d in the main text corresponds to two line-cuts at $B_z = 0.5$ T and $B_z = 1.0$ T.

-
- [1] Manucharyan, V. E., Koch, J., Glazman, L. I. & Devoret, M. H. Fluxonium: Single Cooper-pair circuit free of charge offsets. *Science* **326**, 113–116 (2009).
- [2] Smith, W. C. *et al.* Quantization of inductively shunted superconducting circuits. *Phys. Rev. B* **94**, 144507 (2016).